Materials Advances

ROYAL SOCIETY OF CHEMISTRY

PAPER

View Article Online
View Journal | View Issue

Cite this: *Mater. Adv.*, 2023, 4, 4494

Pressure-dependent comparative study of the mechanical, electronic, and optical properties of $CsPbX_3$ (X = Cl, Br, I): a DFT study for optoelectronic applications†

M. Aktary, *[a] M. Kamruzzaman *[b] and R. Afrose[b]

Inorganic metal-halide perovskite (MHP) materials are potential candidates for optoelectronic and energy-storage device applications. In this work, a systematic hydrostatic pressure-dependent investigation of the elastic, electronic, optical, and photocatalytic properties of $CsPbX_3$ (X = Cl, Br and I) was performed based on *ab initio* simulations. This study revealed that the mechanical stability of Cl- and Br-containing perovskites could be sustained up to 20 and 25 GPa, respectively, while $CsPbI_3$ could survive up to 75 GPa applied pressure. It was also found that the mechanical properties of $CsPbX_3$ perovskites were ductile under ambient conditions and their ductility significantly improved (decreased) with pressure. The electronic property calculations suggested that $CsPbX_3$ perovskites have a direct energy band gap, which decreases with increasing pressure due to structural change and/or a shifting of the conduction band minimum toward the Fermi level. The band gap became zero under pressures of 20.0, 15.0, and 10.0 GPa for Cl-, Br-, and I-based halides, indicating the transition of the crystal structure. The absorption peak of $CsPbX_3$ perovskites radically shifted toward the low photon energy region with applied pressure. The photoconductivity, reflectivity, and dielectric constant showed an increasing tendency under pressure. These findings would be beneficial for experimental study and suggest that pressure has significant effect on the physical properties of $CsPbX_3$ perovskites, which might be a promising avenue for exploitation in optoelectronic and photonic applications.

Received 16th June 2023,
Accepted 19th August 2023

DOI: 10.1039/d3ma00311f

rsc.li/materials-advances

1. Introduction

With a growing global population and a worsening energy problem, demands for more efficient PV cells, optoelectronics, and electronic devices have become a major concern.[1] Researchers are highly concerned about the health of ecosystems because of the pressure from rising demands on resources. The demand for innovative forms of efficient, environmentally friendly, and renewable energy-harvesting technology has attracted a lot of interest from the scientific community.[2–11] To this end, photovoltaic technology has attracted the most research interest for solving the aforementioned problems. Photovoltaic device can directly convert renewable solar energy into electrical energy. It is well known that Si-based solar cells currently dominate the photovoltaic market[12,13] but due to their low efficiency and high maintenance costs of the purification process, this may not last for very long.[1] These involve the use of an indirect band gap semiconductor but reduced optical absorption and carrier mobility have made it uncompetitive for use in more functional devices. Though, amorphous Si technology is both affordable and easy to manufacture, its poor stability and low photoconversion efficiency (PCE) are major causes of concern.[14,15] However, the alternatives to Si, including some inorganic photovoltaic materials, such as iron disulfide (FeS_2), gallium arsenide (GaAs), and cadmium telluride (CdTe), are promising but their efficiency is not yet satisfactory. Multi-junction AlGaInP-, AlGaAs-, GaAs-, and GaInAs-based solar cells are another alternative, and being around 47.1% more efficient have attracted a great deal of attention from the scientific community.[16] Although, current research is encouraging, all these mixtures are expensive due to the inclusion of scarce elements, such as In or Ga, and also hazardous due to the prescence of As and P. As a result, scientists are keen to identify new solar cell materials that are inexpensive, abundant on earth, and easily processed. To this goal, organic–inorganic halide perovskites are of tremendous interest as they fulfill

[a] *Department of Materials Science and Engineering, King Fahd University of Petroleum and Minerals, Saudi Arabia. E-mail: aktarymahbuba@gmail.com; Tel: +966 532754870*
[b] *Department of Physics, Begum Rokeya University, Rangpur, Rangpur-5400, Bangladesh. E-mail: kzaman.phy11@gmail.com*

† The author is dedicating this article to her beloved friends Popy, Pritha, Shahina and Dana.

these requirements. Extended research into the development of perovskites began in the 1990s with an aim to replace Si and to produce multipurpose solar cell technology. Miyasaka and co-workers introduced a perovskites solar cell in 2006 for the first time, with a PCE of 2.2%,[17] which had reached 3.8% by 2009.[18] Researchers reported a much increased PCE of 27.6% in 2018, while the US National Renewable Energy Laboratory verified a perovskite solar cell with a maximum PCE of 25.5% in 2020.[19] Thus, by carefully choosing the right atoms and placing them in the right places, metal-halide perovskites solar cells have a great chance of replacing the dominant Si-based solar cells.[20–25] Organic–inorganic halide perovskites with the formula ABX_3 (where, A = monovalent organic–inorganic cation, reported as Cs^+ or CH_3NH^{3+}, *etc.*; B = a divalent inorganic cation: Pb^{2+} or Sn^{2+} *etc.*; X = a halide: Cl-, Br-, I-)[1] are highly efficient[26–29] due to their excellent absorption coefficient,[30–32] carrier mobility, long carrier life, and suitable band gaps.[33–36]

Inorganic perovskites have received a lot of attention from researchers despite the fact that organic–inorganic perovskites are physically and chemically not very stable.[1] For the next generation of advanced electrical, optoelectronic, and other devices, Cs-based inorganic perovskites $CsPbX_3$ (X = Cl, Br, I) are considered the most promising materials.[37]

To improve the performance of optoelectronic devices, like LEDs, photodetectors, and lasers, the characteristics of $CsPbX_3$ need to be modified by adding metal halides or combining with halides.[38–59] Due to its higher binding energy of 64 meV, $CsPbCl_3$ (X = Cl, Br, I) has a larger band gap and superior thermal stability, making it the preferred choice for many optomagnetic and optoelectronic,[60] single,[61] and multiphoton pumping-based laser devices.[62] $CsPbBr_3$ has demonstrated a band gap of 3.153 eV,[62] and cubic bulk $CsPbI_3$ a band gap of 1.73 eV.[4] It has been shown that direct band gap semiconductors with the formula of $CsPbX_3$ (X = Cl, Br, I) absorb visible and ultraviolet light. As perovskites are a smart class of materials with significant potential for photovoltaic and optoelectronic applications, all-inorganic perovskites have a very flexible crystal structure and are attracting great interest.

As pressure is a key factor in adjusting the physical characteristics of any material,[63–65] by adjusting the pressure, the optical, electronic, and optoelectronic properties can be tuned as well as the material phase transitions.[66–70] For example, Zou *et al.* (2017) reported that at considerably greater pressures, the Jahn–Teller effect might eventually result in a direct to indirect band-gap electrical transition.[71] This research established high pressure as a reliable tool for controlling the

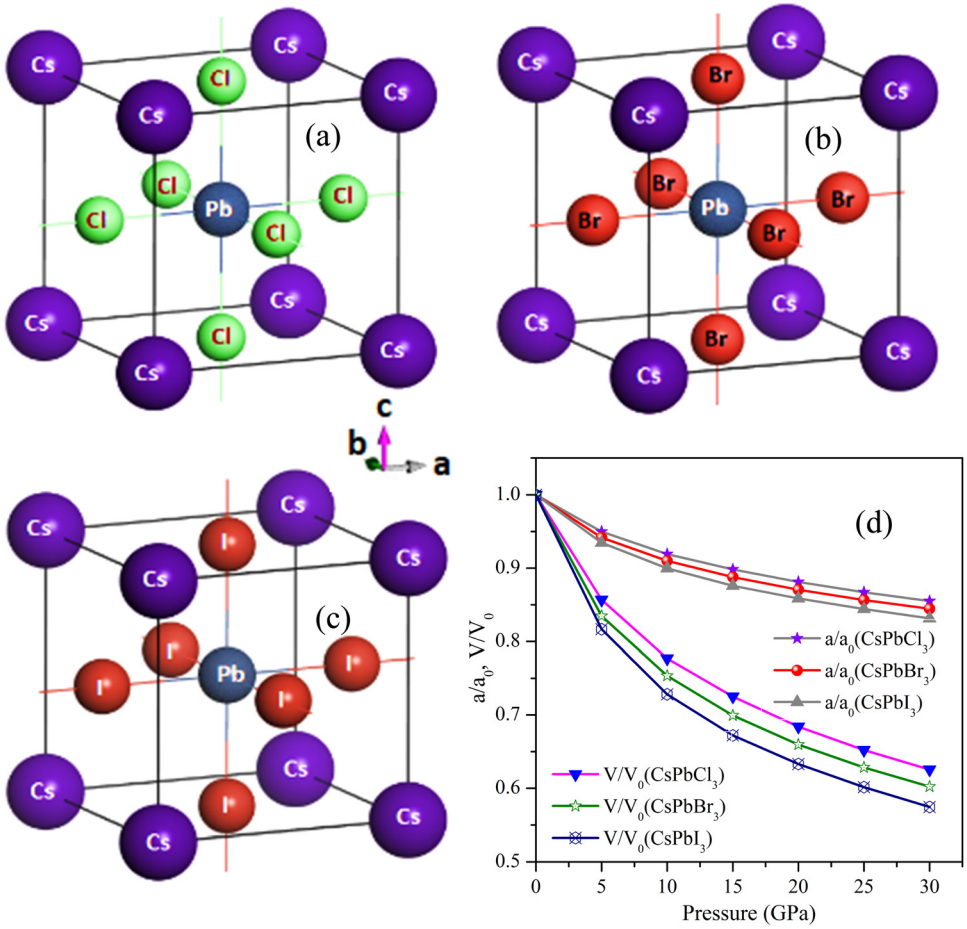

Fig. 1 Pressure response for the structures of (a) $CsPbCl_3$ (b) $CsPbBr_3$, and (c) $CsPbI_3$ depicted with their atomic orientations.

structure along with the band gap of $CsPbBr_3$ NCs, revealing the nano-scale physiochemical process of these squeezed MHP nanosystems. So, the pressure-dependent properties are crucial for optoelectronic quantum dot applications. In this way, research conducted under high pressure frequently provides insights into the optoelectronic characteristics of perovskite materials for photoluminescence kinetics.

However, extensive theoretical research on the pressure-dependent comparisons of the elastic, mechanical, electronic, and optical characteristics of $CsPbX_3$ has not yet been published. The compound is more beneficial for applications in optoelectronic devices thanks to the tuning of the band gap, which can improve electron movement from the valence band to the conduction band, boosting the optical absorption and conductivity.

2. Method

The lattice constants of bulk perovskites of $CsPbX_3$ (X = Cl, Br, I) are 5.734, 6.017, and 6.38 Å, respectively, and they have a cubic structure with the space group *Pmm* (221) (Table 5). DFT calculations were carried out using the CASTEP code in the Materials Studio simulation software to compare and analyze the results of the structural, mechanical, electronic, and optical properties.[72–77] Electrostatic interactions between component atoms' valence shell and ion core were examined using the Perdew–Burke–Ernzerhof (PBE) in the framework of the generalized gradient approximation (GGA) and ultrasoft pseudopotentials. Electronic band edge diagram calculations were also used to calculate the photocatalytic property. To begin with, we decided to perform numerical operations on a cubic structure.

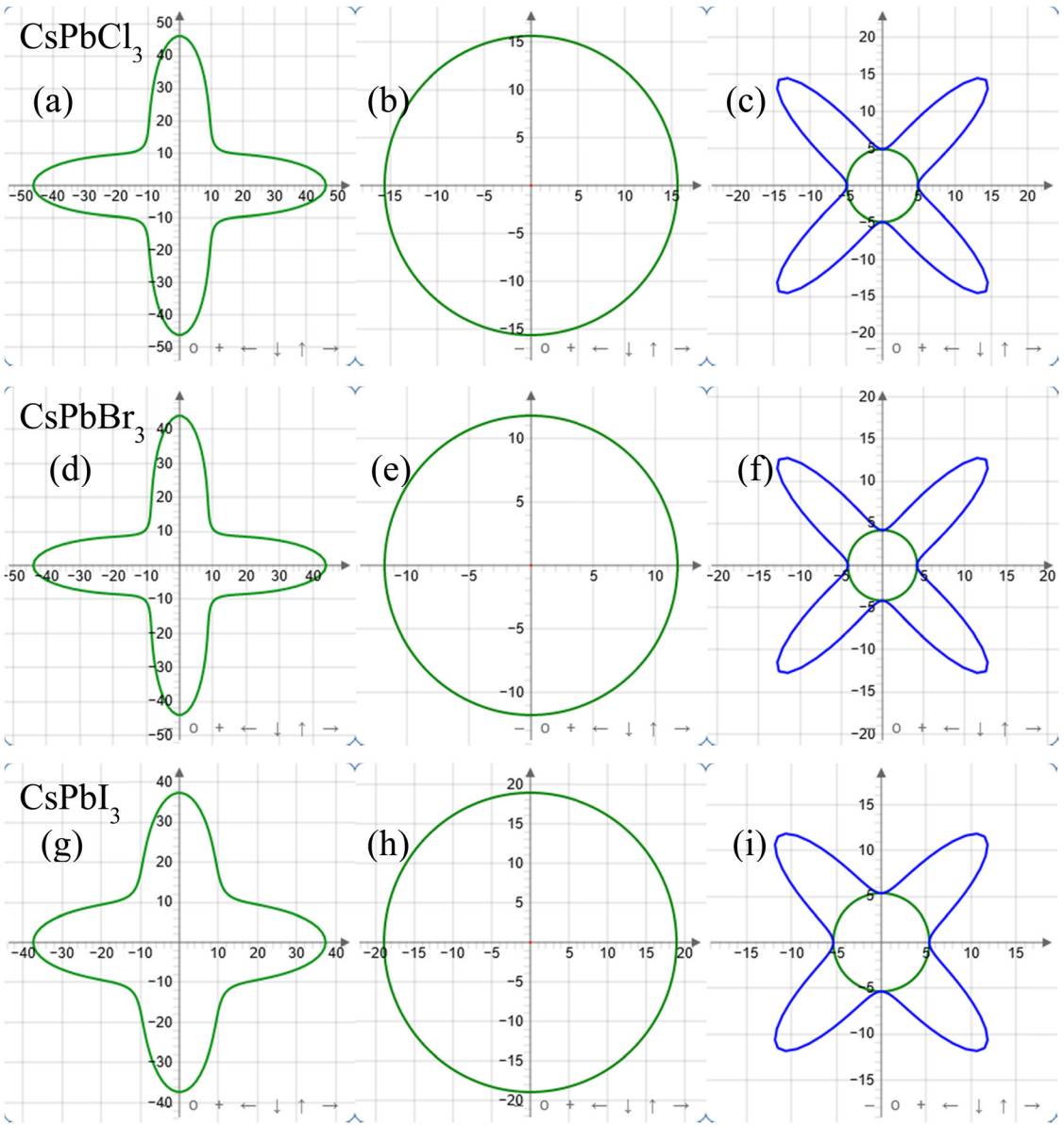

Fig. 2 2D representation of the Young's modulus (a) and (d), (g), linear compressibility (b) and (e), (h), and shear modulus (c), (f) and (i) plotted in the *xy*-plane with ELATE code for $CsPbX_3$ at zero pressure.

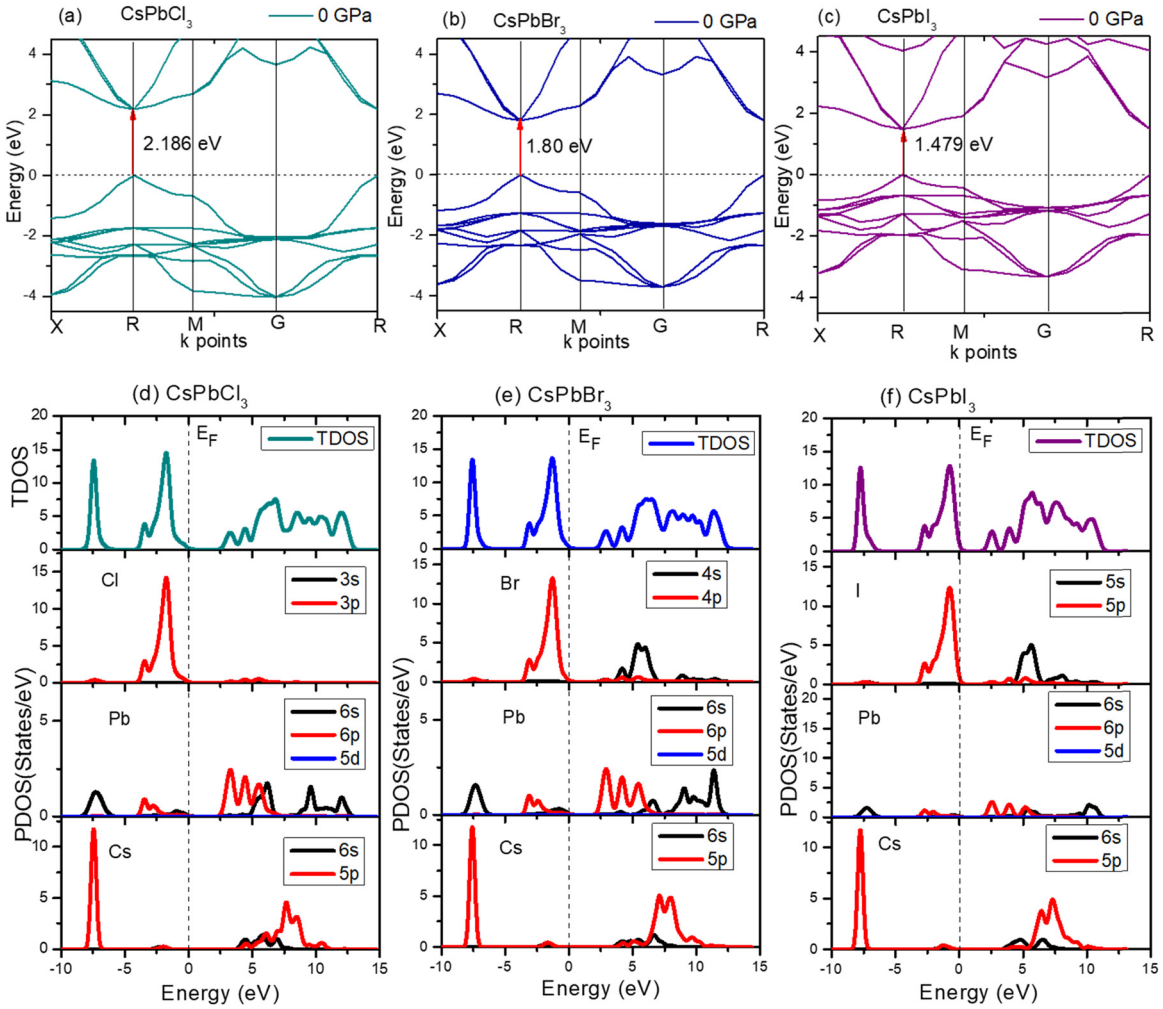

Fig. 3 Energy band diagram with k-points for (a) $CsPbCl_3$, (b) $CsPbBr_3$, and (c) $CsPbI_3$, and density of states (DOS) with the corresponding energies of the constituent atoms of (d) $CsPbCl_3$, (e) $CsPbBr_3$, and (f) $CsPbI_3$ as calculated by GGA-PBE treatment.

A five-atom $CsPbCl_3$ primitive cell was thus developed, as shown in Fig. 1. In this cell, one Cs atom is located at the Wyckoff site (0, 0, 0), one Pb atom is located at the site of (0.5, 0.5, 0.5), and three Cl atoms are located at (0, 0.5, 0.5) fractional coordinates. The valence sets interact as follows: Cs: $5s^2\ 5p^6\ 6s^1$, Pb: $5s^2\ 5p^6\ 5d^{10}\ 6s^2\ 6p^2$, Cl: $3s^2\ 3p^5$, Br: $4s^2\ 4p^5$, and I: $5s^2\ 5p^5$. Identical software functional treatments were used to optimize all the crystals. $CsPbCl_3$ was first simulated with the lattice parameter set to a = 5.734 Å.[78] The optimized structure with the lowest formation enthalpy was then verified with the plane-wave basic set and k-points of 6 × 6 × 6 and a 520 eV cutoff energy, SCF tolerance of 2×10^{-6} eV per atom, convergence tolerance energy of 2×10^{-5} eV per atom, and maximum force and stress of 0.05 eV $Å^{-1}$ and 0 GPa, respectively. The largest atomic displacement was limited to 0.002.

After substituting Br and I atoms (100%) for the Cl atoms in $CsPbBr_3$ and $CsPbI_3$ under the same conditions, we determined the elastic, electrical, and optical properties of each compound.

3. Results and discussion

3.1 Structural and mechanical properties

To do the numerical calculations, we mostly chose the cubic structure of $CsPbCl_3$ among cubic, tetragonal, and orthorhombic structures due to its high-temperature tolerance. In order to achieve structural analysis, like to obtain the lattice constant, a (Å), bulk moduli, B (GPa), and its pressure responses, the volume of the unit cell of each $CsPbX_3$ (X = Cl, Br, I) was tuned by optimization of the parameters. After discovering the $CsPbCl_3$ cell's optimized structure, the Cl atom was substituted

Table 1 Calculated pressure-independent (at 0 GPa) elastic constants C_{ij} (GPa), elastic moduli B, G, E (GPa), and Poisson's ratio σ for $CsPbCl_3$, $CsPbBr_3$, and $CsPbI_3$

Materials	C_{11}	C_{12}	C_{44}	B	G	E	σ
$CsPbCl_3$	48.35	7.88	4.92	21.37	9.05	23.79	0.31
$CsPbBr_3$	51.94	16.47	4.18	28.30	7.81	21.47	0.37
$CsPbI_3$	39.32	6.75	5.35	17.61	8.52	22.01	0.29

Table 2 Calculated elastic constants C_{ij} (GPa) for $CsPbCl_3$, $CsPbBr_3$, and $CsPbI_3$ in norm-conserving and ultrasoft pseudopotentials

Elastic constants	C_{11}		C_{12}		C_{44}	
Pseudopotential	Norm-conserving	Ultrasoft	Norm-conserving	Ultrasoft	Norm-conserving	Ultrasoft
$CsPbCl_3$	20.3	39.32	−9.178	6.75	7.589	5.35
$CsPbBr_3$	22.699	51.94	−6.928	16.47	5.487	4.18
$CsPbI_3$	14.923	48.35	−5.519	7.88	4.511	4.92

Table 3 Calculated pressure-dependent lattice constant a (Å) and elastic constants C_{ij} (GPa) for $CsPbI_3$, $CsPbBr_3$, and $CsPbCl_3$

Materials	$CsPbI_3$				$CsPbBr_3$				$CsPbCl_3$			
P (GPa)	a (Å)	C_{11}	C_{12}	C_{44}	a (Å)	C_{11}	C_{12}	C_{44}	a (Å)	C_{11}	C_{12}	C_{44}
0	6.4	39.32	6.75	5.35	6.01	51.94	16.47	4.18	5.73	48.35	7.88	4.92
5	5.98	81.66	12.25	4.67	5.66	90.46	13.99	3.61	5.44	97.06	16.58	4.06
10	5.76	119.43	15.97	1.34	5.47	125.74	14.11	2.88	5.27	145.49	29.86	2.91
15	5.6	170.4	27.37	6.43	5.33	173.83	28.69	2.14	5.15	175.01	27.9	1.68
20	5.49	207.43	35.46	5.79	5.23	211.2	35.27	1.28	5.05	214.4	36.14	0.48
25	5.4	238.25	38.76	3.17	5.15	248.17	43.08	0.33	4.97	249.95	43.19	−0.71
30	5.32	288.88	50.85	7.06	5.07	283.31	49.76	−0.66	—	—	—	—
35	5.25	323.53	58.81	6.71	—	—	—	—	—	—	—	—
40	5.2	357.61	66.84	6.36	—	—	—	—	—	—	—	—
45	5.15	388.58	72.78	5.46	—	—	—	—	—	—	—	—
50	5.1	419.99	79.41	3.5	—	—	—	—	—	—	—	—
55	5.06	449.5	84.78	1.32	—	—	—	—	—	—	—	—
60	5.02	483.76	93.12	0.97	—	—	—	—	—	—	—	—
65	4.98	523.28	103.91	3.34	—	—	—	—	—	—	—	—
70	4.95	560.19	114.31	4.65	—	—	—	—	—	—	—	—
75	4.92	588.96	119.87	2.62	—	—	—	—	—	—	—	—
80	4.89	615	124.42	−0.96	—	—	—	—	—	—	—	—

Table 4 Calculated band gap of $CsPbX_3$ in norm-conserving and ultrasoft pseudopotentials

Materials	E_g (eV) (ultrasoft)	E_g (eV) (norm)	E_g (eV) (experiment)
$CsPbCl_3$	2.186	2.385[a]	2.98[b]
$CsPbBr_3$	1.80	2.061[a]	2.36[b]
$CsPbI_3$	1.479	1.784[a]	1.77[b]

[a] Ref. 79. [b] Ref. 84.

Table 5 Calculated optimized lattice parameters, volumes, and band gap values of $CsPbCl_3$, $CsPbBr_3$, and $CsPbI_3$ with applied pressure

Materials	Method	P (GPa)	Lattice parameters		Band gap	Bulk
			a (Å)	V (Å^3)	E_g (eV)	type
$CsPbCl_3$	Calc.	0	5.734	188	2.186	Cubic
		5	5.446	161	1.463	
		10	5.271	146	0.836	
		15	5.151	136	0.311	
		20	5.052	128	0	
$CsPbBr_3$	Calc.	0	6.014	217	1.80	Cubic
		5	5.663	181	1.008	
		10	5.473	163	0.384	
		15	5.339	152	0	
$CsPbI_3$	Calc.	0	6.403	262	1.479	Cubic
		5	5.985	214	0.715	
		10	5.761	191	0.125	
		15	5.608	176	0	

for the Br and I atoms, which made the cell optimized for the $CsPbBr_3$ and $CsPbI_3$ perovskite structures. The optimized crystal structures, normalized parameters, and volumetric pressure responses of $CsPbCl_3$, $CsPbBr_3$, and $CsPbI_3$ are shown in Fig. 1(a)–(d) and Table 5 shows the optimal cell parameters for the matching perovskites. From Table 5, it can be seen that $CsPbCl_3$'s optimum lattice parameter a was 5.734 Å, which was elongated by 4.8% and 11.6%, respectively, after the replacement of the Cl atom by Br and I atoms. It was seen that the optimized lattice parameter a decreased to 5.02%, 8.07%, 10.1%, and 11.8% for $CsPbCl_3$ as the pressure was increased to 5, 10, 15, and 20 GPa, respectively. For $CsPbBr_3$ and $CsPbI_3$, the decrement was 5.8% and 6.5% at 5 GPa, 8.9% and 10.0% at 10 GPa, and 13.3% and 12.4% at 15 GPa, respectively, as result of the replacement of the halide Cl atom by Br and I atoms. The resulting values were in good accordance with other theoretical as well as experimental results reported.[79] From these results for $CsPbX_3$ (X = Cl, Br, I), a relation was established and can be expressed as: $V_{CsPbCl_3} < V_{CsPbBr_3} < V_{CsPbI_3}$ (Table 5) with a volume increment of 15.4% and 39.3% for $CsPbBr_3$ and $CsPbI_3$, respectively, as a result of lattice expansion due to the comparatively larger ionic radii of Br and I atoms.

Three separate elastic tensors, C_{11}, C_{12}, and C_{44}, were used to independently calculate the explicit and implicit mechanical properties of the cubic perovskites of $CsPbX_3$. The computed values for the isostructural forms of $CsPbCl_3$, $CsPbBr_3$, and $CsPbI_3$ are displayed visually in Fig. 2(a) and recorded in Table 1. From Fig. 2(a) and Table 1, it is obvious that they were

mechanically stable because all these crystals met the conditions of $C_{11} + 2C_{12} > 0$, $C_{44} > 0$ and $C_{11} - C_{44} > 0$ as well as the additional stability criterion of $C_{12} < B < C_{11}$.[80] The mechanical stability was justified under Born's criteria for these crystals.[81] The association of $2C_{44} = C_{11} - C_{12}$[82] and a non-zero Zener's anisotropy factor A both demonstrated that each of these bulks was elastically anisotropic.[83] The materials exhibited greater resistance to longitudinal deformation than to shape deformation under the circumstances of $C_{11} > C_{12} > C_{44}$, with $CsPbBr_3$ having the highest value of C_{11}. The capacity of materials scientists to create novel materials with specific mechanical reactions is constrained by the absence of experimental data. With anisotropic materials, it is much more important to examine and depict the directional elastic characteristics as opposed to their averages, such as Young's modulus, linear compressibility, shear modulus, and Poisson's ratio. At the threshold value of Poisson's ratio 0.26 (known as brittle/ductile borderline), the material can be distinguished as a brittle or ductile crystalline material. Table 1 makes it very obvious that the $CsPbX_3$ materials had values larger than 0.26, proving their high degree of ductility. Among them, CsPbI3 was more ductile because it could withstand higher pressure.

ELATE Code is a reliable computational method to observe elastic moduli in 2D as well as 3D views. To observe the elastic properties in different crystallographic planes, the Young's modulus, linear compressibility, and shear modulus were plotted with ELATE code only for the zero pressure condition in 2D plane projections. For $CsPbX_3$, all the above-mentioned parameters showed similar responses along the *xy*, *xz*, and *yz* planes. So only the *xy*-plane responses are shown in Fig. 2. The Young's modulus exhibited the highest values along the horizontal and vertical axes, and at least at 45° between the abscissa and ordinate.

The linear compressibility showed direction-independent responses for $CsPbX_3$ (Fig. 2(b), (e) and (h)). According to Fig. 2(c), (f) and (i), the shear modulus showed a direction-based inverse response with Young's modulus. The maximum and minimum anisotropy in the shear modulus were obtained at 45° and in the axial directions respectively.

The negative value of C_{12} presented in Table 2, calculated by the norm-conserving pseudopotential, gave a negative value of Poisson's ratio σ (which is unacceptable) and did not satisfy Born's condition of mechanical stability. That is why this research utilized ultrasoft pseudopotentials. According to this study, iodine-containing perovskites could withstand pressures of up to 75 GPa, whereas the Cl- and Br-containing perovskites could withstand pressures of up to 20 and 25 GPa, respectively, as confirmed by the negative value of C_{44} presented in Table 3.

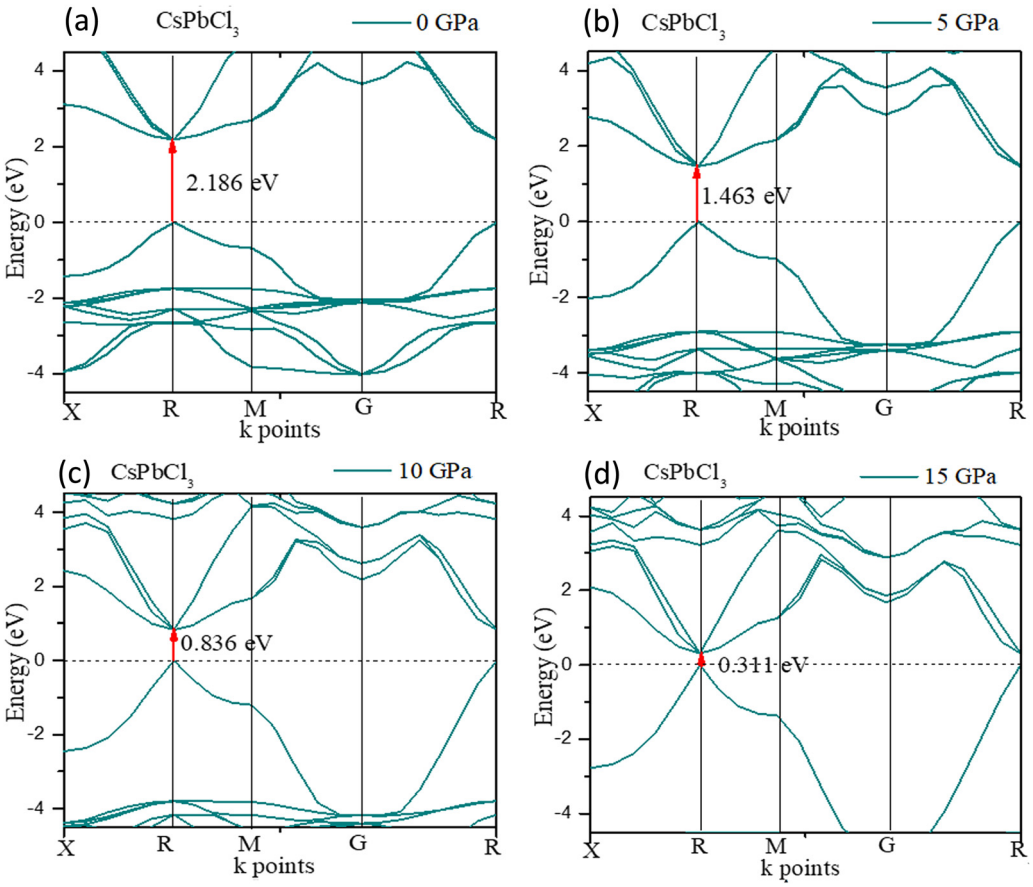

Fig. 4 Calculated band gap values of $CsPbCl_3$ with applied pressure.

3.2 Electronic properties

Table 4 shows the values of E_g, and Table 5 shows the pressure-dependent lattice parameter, volume, and band gap values of $CsPbX_3$.

Though the norm-conserving data for the band gap were closer to the reported experimental values (Table 4), the ultrasoft pseudopotential method provided greater accuracy in the case of the mechanical stability measurement. Material of interest must follow Born's criteria mentioned in Section 3.1 (Structural and mechanical properties), and ultrasoft pseudopotential enabled keeping to that standard (Table 2).

Pressure-dependent electronic properties. The pressure-dependent lattice parameters, including lattice constants and volume, and electronic band gaps till the end of reaching metallic transition are tabulated in Table 5.

The crystal structure could be densified under high pressure with structural renovation. The evolution of the band gap of $CsPbCl_3$ under pressure is shown in Fig. 4. It could be found that the band gap (E_g) decreased with an increase in pressure and finally decreased to zero at 20 GPa pressure.

For $CsPbCl_3$, the direct band gap was 2.186 eV as calculated with the ultrasoft pseudopotential, which was in good agreement with the experimental value.[82] This decreased to 1.463 eV at 5 GPa which is still suitable for photovoltaic applications in tandem solar cells, and is really ideal for high power conversion efficiency single solar cells. In this study, the band gap was reduced to 0 eV at hydrostatic pressures $\leq$ 20 GPa.

To further understand the electronic properties of $CsPbCl_3$ under pressure, the partial density of states (PDOS) of $CsPbCl_3$ were also calculated. The states at the valence band and conduction band near the Fermi level were mainly formed by the hybridization of the Cl-3p and Pb-6p states, respectively. The band gap decreased with the increase in pressure, due to delocalization of the bands and the energy range broadened as the pressure increased.

The electronic structure of $CsPbBr_3$ under pressure was investigated. Fig. 5 displays the variation of the band gap of $CsPbBr_3$ as a function of pressure. The ground state band gap of $CsPbBr_3$ at 0 GPa possessed a value of 1.80 eV, but the band gap decreased with the increase in pressure, which was similar to the experimental results. From Fig. 5, it could be clearly seen that the band gap of the cubic $CsPbBr_3$ decreased with the increasing pressure, and ultimately reached 0 eV at 15 GPa. The lattice parameter a also reached a smaller value compared to at 0 GPa, and showed a similar variation to the band gap when the pressure increased (Table 5).

The expansion and/or shrinkage of the lattice parameter a may shift the bands and change the band gaps. The minimum of the lattice parameter 'a' caused the band gap to reach the

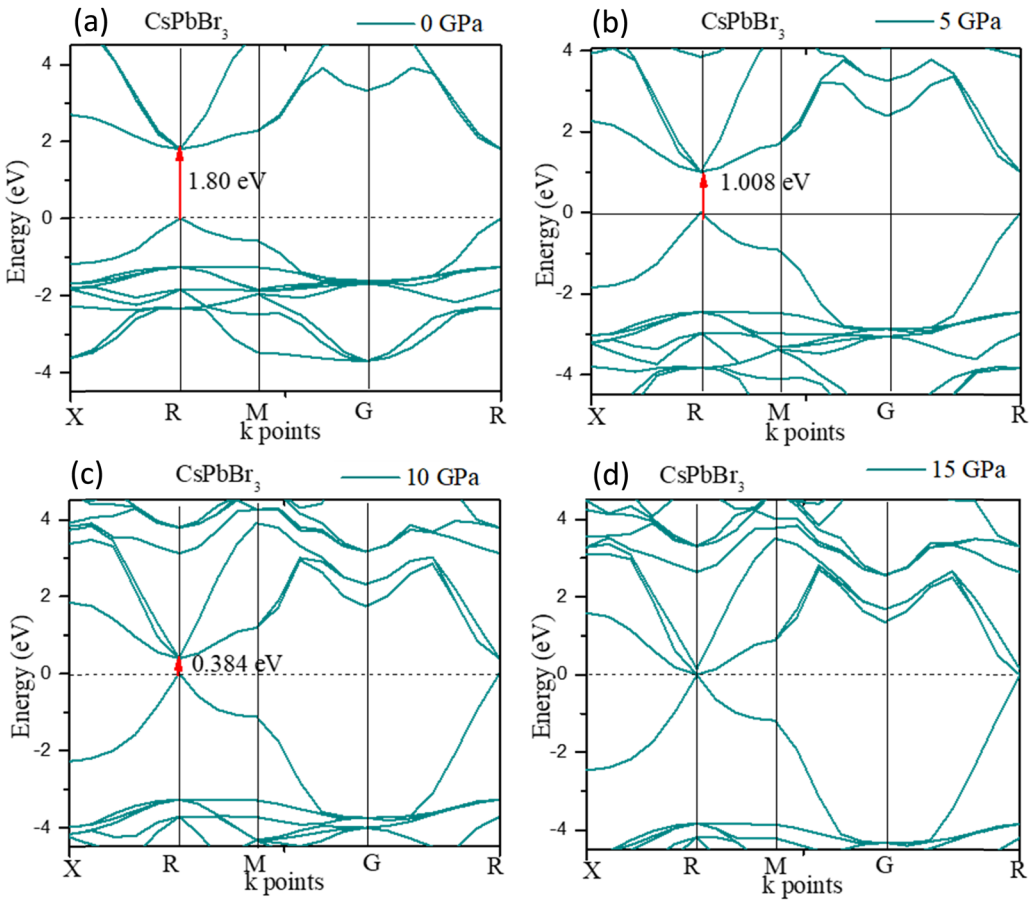

Fig. 5 Calculated band gap value of $CsPbBr_3$ with applied pressure.

minimum value. The band gap could change to zero and $CsPbBr_3$ could become metallic if the pressure was further increased.

Fig. 6 shows the band gap of cubic $CsPbI_3$. The band gap was 1.479 eV at 0 GPa, which decreases to 0 eV at $\leq$15 GPa. The deviation of the band gap was associated with the lattice parameter '*a*', which slightly decreased from 0 to 15 GPa, as shown in Fig. 6(c).

The high-pressure structure had a greater electronic charge density overlap between the Pb and X (= Cl, Br, I) atoms than the ambient structure. The CBM mostly exhibited a nonbonding Pb 6p character, while the VBM could be classified as an antibonding hybridized state, consisting of p orbitals of X (= Cl, Br, I) and a tiny number of Pb 6s orbitals. It was amazing that the electronic levels from the Cs^+ cations were positioned far from the VBM and CBM (Fig. 3); as a result, they could only compensate for the charge valence and did not directly contribute to the band edge states, suggesting that PbX_6 octahedra primarily control the optoelectronic properties of $CsPbX_3$. Compression of the Pb–X bond strengthened the coupling between the X p and Pb 6s orbitals, which raised the VBM and increased band dispersion. The CBM was not responsive to pressure when it was mostly in a nonbonding localized condition. By pushing the VBM higher, the enhanced orbital coupling reduced the band gap.

3.3 Optical properties

The potential use of a material in optoelectronic devices depends on its pressure-dependent optical characteristics. There have been several papers on the optical characteristics of perovskites, but none have compared the optical properties of $CsPbX_3$, which are highly relevant since they are used in thin-film transistors and solar cells. For this reason, here we studied the pressure-dependent optical properties (absorption, photoconductivity, reflectivity, refractive index, and the real and imaginary parts of the dielectric function) of $CsPbX_3$ for many application fields. Such applications of material depend on its optical responses. The photonic interaction of a material can provide light on the perspective, characteristics, and application forecasts as a function of energy when there are external electromagnetic waves present. Owing to their optical spectra, these features were examined for electrical shifts between filled and vacant states, band constructions, bond types, and the internal structure of the materials. The Kramers–Kronig transformation was followed by the frequency-dependent complex dielectric function, which is connected to the demonstration of relative permittivity and has the formula $\varepsilon(\omega) = \varepsilon_1(\omega) + i\varepsilon_2(\omega)$. The imaginary

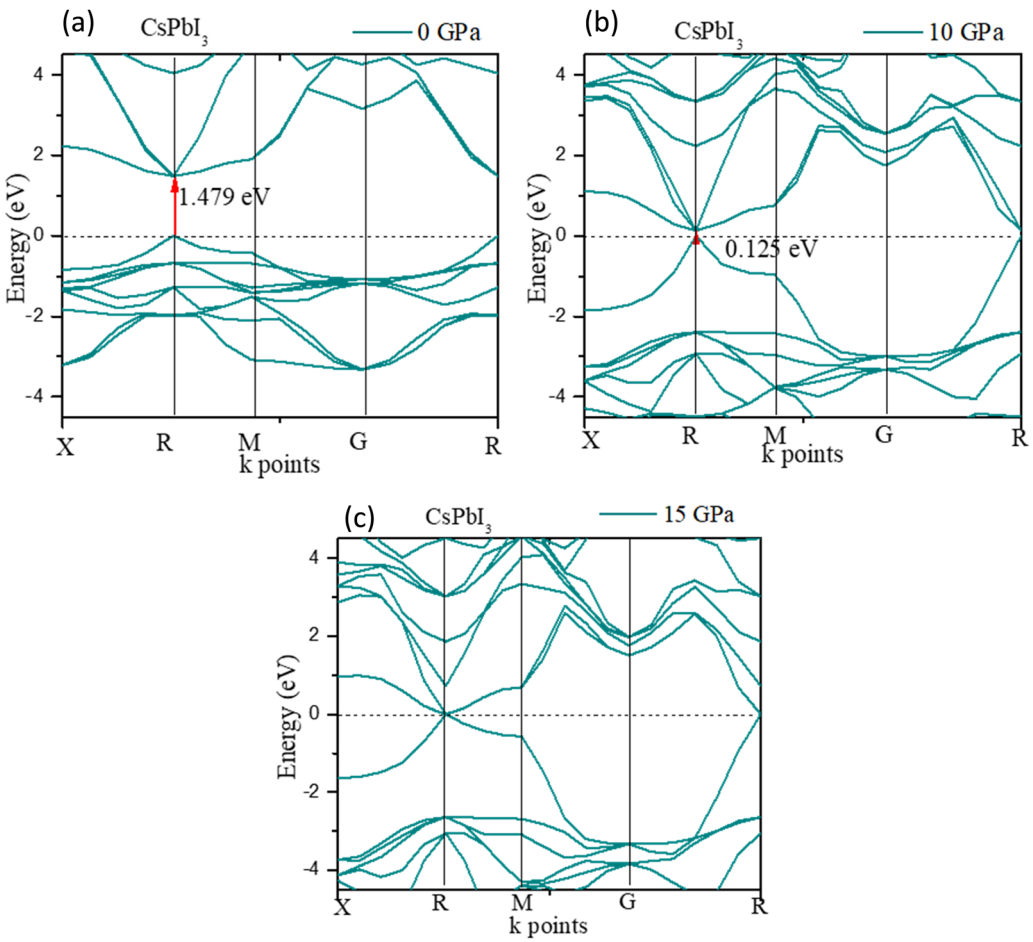

Fig. 6 Calculated band gap values of $CsPbI_3$ with applied pressure.

portion of this complex dielectric function is,

$$\varepsilon_2(\omega) = \frac{2e^2\pi}{\Omega\varepsilon_0}\sum_{k,v,c} k\Psi_k^c|\hat{u}.\hat{r}|\Psi_k^v||^2\delta\left(E_k^c\right) - E_k^v - (E)$$

where $\omega = 2\pi\nu$ is the angular frequency of an incoming photon; and e, $\hat{r}$ and $\hat{u}$ are the electronic charge, radius vector, and polarization vector of the incident field, respectively; whereas, Ψ_k^c and Ψ_k^v represent the wave functions of the conduction band and valence band at k, respectively. Optical properties, such as absorption, conductivity, loss function.reflectivity, and refractive index can be calculated explicitly in terms of ε_1 and ε_2[85] as,

$$\sigma(\omega) = \frac{\omega\varepsilon_2}{4\pi} = \hbar\omega$$

$$L(\omega) = \frac{\varepsilon_2(\omega)}{\varepsilon_1(\omega)^2 + \varepsilon_2(\omega)^2}$$

$$R(\omega) = \left|\frac{\sqrt{\varepsilon}(\omega) - 1}{\sqrt{\varepsilon}(\omega) + 1}\right|^2$$

$$n(\omega) = \left|\frac{\varepsilon_1(\omega)}{2} + \frac{\sqrt{\varepsilon_1(\omega)^2 + \varepsilon_2(\omega)^2}}{2}\right|^{\frac{1}{2}}$$

The charge-carrier recombination rate of specific materials used in solar cells is affected by a basic characteristic known as the dielectric function.[86,87] It provides a precise understanding of how optoelectronic devices function.[88] Lower recombination rates are revealed by perovskite solar cells with higher dielectric constant values.

Pressure-dependent optical properties. The pressure-dependent optical properties are crucial for their potential applications in optoelectronic devices. There are various reports on the optical properties of perovskite materials; however, so far there is no such comparative analysis of the pressure-dependent optical properties of $CsPbX_3$, which would be quite significant because of their applications in solar cells and thin films transistor, *etc.* For this reason, here we studied the pressure-dependent optical properties (absorption, photoconductivity, reflectivity, refractive index, and dielectric function) of $CsPbX_3$ for many application fields.

Fig. 7(a) and (b) show the pressure-dependent real and imaginary parts of the dielectric function of $CsPbX_3$ perovskites. The real part of the dielectric function (Fig. 7(a)) showed a higher value at low photon energy and then decreased rapidly with the increase in photon energy. Whereas the pressure-induced perovskite exhibited a higher dielectric constant in

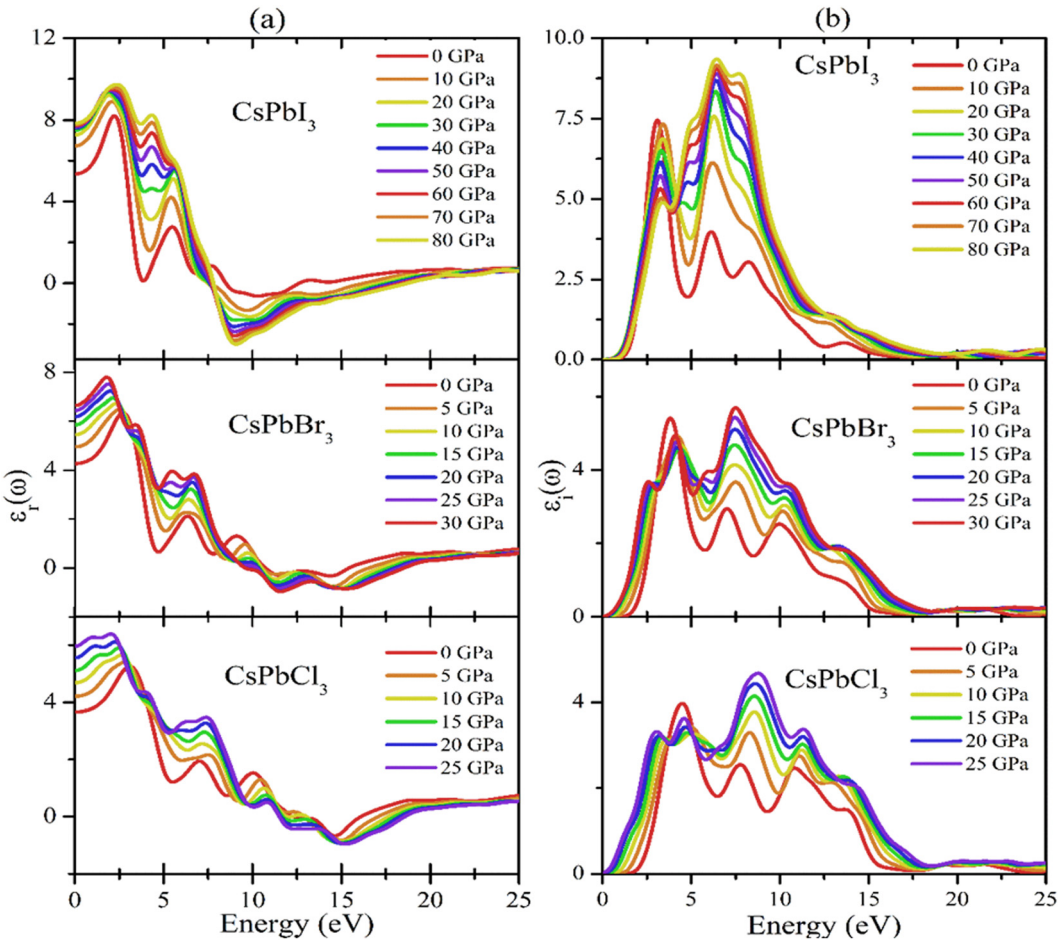

Fig. 7 Optical responses in terms of the dielectric function of $CsPbX_3$.

the visible range. It is well known that normally a perovskite material with such a higher value of the real part of the dielectric function would exhibit a lower band gap,[89] which is related to the Penn model. It could also be seen in the electronic band structure (shown in Fig. 3 and 7(b)) that the band gap decreased with increase in applied pressure, which was consistent with the behavior of the imaginary part of the dielectric function. It was evident that the imaginary part dielectric function could be correlated with the optical absorption/transition and the material's band gap. It could be found that the values of the imaginary part of the dielectric function were enhanced with applied pressure and the peaks were shifted toward the lower incident photon energy, which was similar to the optical absorption in Fig. 8(a). On the other hand, the values of the imaginary part of the dielectric function decreased to zero in the higher photon energy region.

It is well known that the performance of solar cells is determined by various optical properties, among which the absorption coefficient (α) is the crucial property. The variation of the optical absorption of $CsPbX_3$ perovskites with pressure can be seen in Fig. 8(a). It could be clearly seen that the optical absorption edge of cubic $CsPbX_3$ perovskites was shifted to the low energy region, indicating a shifting of the band gap with applied pressure within the visible range. Furthermore, the value of α of the I-based perovskite demonstrated the maximum intensity in the ultraviolet region, rather than the Br- and Cl-based perovskites. The width of the absorption peak of $CsPbI_3$ was higher than that of $CsPbCl_3$ and $CsPbBr_3$ in the UV region. Fig. 8(b) shows the pressure-dependent real part of the photoconductivity. From the figure, it is evident that when the absorption of photons is enhanced, the rate of photoconductivity tended to increase. Thereby the greater absorption and photoconductivity that could be observed in the I-based perovskite compound could be due to lower band gap relative to the Br- and Cl-based perovskite compounds with applied pressure.

Reflectivity is an important optical property that determines the surface nature of materials for optoelectronic and solar cell applications.[90] Fig. 9(a) shows the pressure-dependent reflectivity spectra of the $CsPbX_3$ perovskites. From these graphs, it can be seen that at zero pressure the reflectivity was very low for all the studied cubic perovskite compounds. Then, when pressure was applied, the value of the reflectivity and loss function increased significantly with the increase in

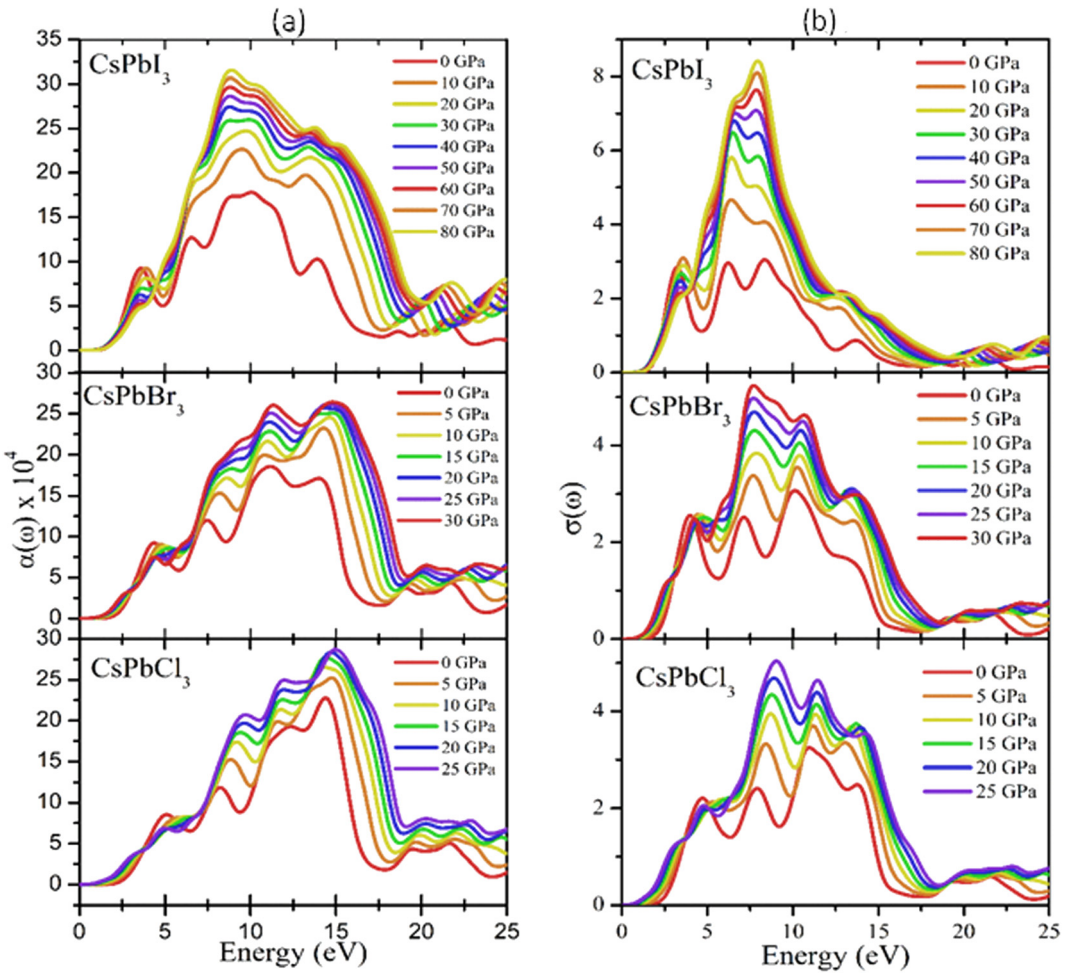

Fig. 8 Optical responses in terms of the (a) absorption coefficients and (b) conductivity of $CsPbX_3$.

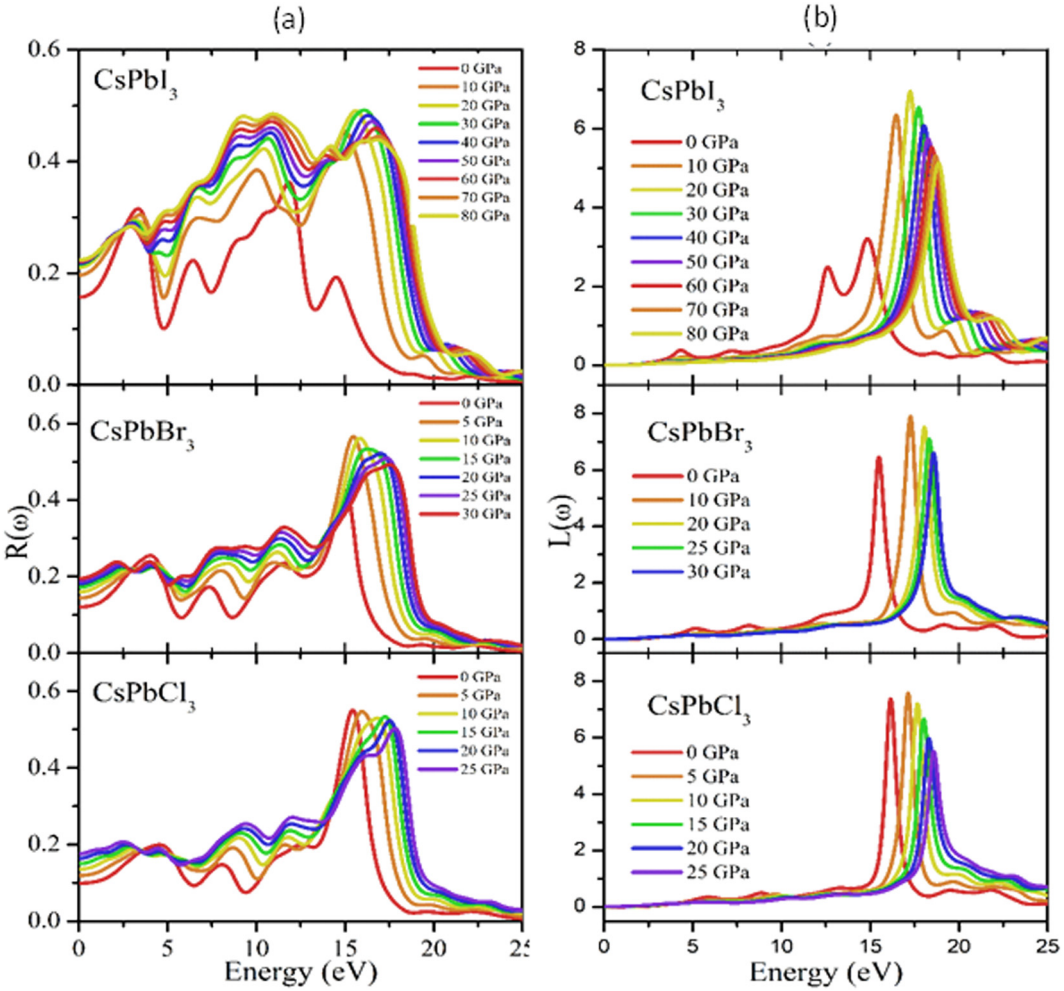

Fig. 9 Optical responses in terms of the (a) reflectivity and (b) loss function of $CsPbX_3$.

applied pressure, which could be due to changes of the band gap and/or structure (Fig. 9(a) and (b)).

Fig. 7(a) and (b) show the pressure-dependent real and imaginary parts of the dielectric function of $CsPbX_3$ perovskites. The real part of the dielectric function (Fig. 7a) showed a higher value with low photon energy and then decreased rapidly with the increase in photon energy. Whereas the pressure-induced perovskite exhibited a higher dielectric constant in the visible range. It is well known that normally a perovskite material with such a higher value of the real part of the dielectric function would exhibit a lower band gap.[91] This could also be seen in the electronic band structure in Fig. 3. Fig. 7(b) shows the behavior of the imaginary part of the dielectric function with the applied pressure. The imaginary part of the dielectric function was correlated with the optical absorption and the material's band gap. It could be found that the values of the imaginary part of the dielectric function was enhanced with applied pressure and the peaks were shifted toward lower incident photon energy, which was similar to the optical absorption in Fig. 8(a). On the other hand, the values of the imaginary part of the dielectric function decreased to zero in the higher photon energy region. It should be noted that a few peaks appeared at 3.9, 7.8, 11.0, and 14.1 eV for $CsPbCl_3$; 3.5, 7.3, 10.3, and 13.9 eV for $CsPbBr_3$; and 3.0, 6.3, 8.5, and 13.9 eV for $CsPbI_3$. The first peak was due to the generation of electron–hole pairs for conduction. The 2nd and 3rd peaks were due to interband optical transitions from the valence bands to the conduction bands. The fourth peak around 14.0 eV was due to collecting excitons of the free carriers, which is the so-called plasma frequency and the peak is called the plasmon peak. These irregular photoresponses of the materials caused the differences in the band gaps among them.

It is well known that the performance of solar cells is determined by various optical properties, among them absorption coefficient (α) is the crucial property. The variation of optical absorption of $CsPbX_3$ perovskites with pressure can be seen in Fig. 8(a). It is clearly seen that the optical absorption edge of cubic $CsPbX_3$ perovskites is shifted to the low energy region with applied pressure within the visible ranges. In Fig. 8(a) the absorption edges are remarkably enhanced under pressure within the visible ranges. Furthermore, the value of α of the I-based perovskite demonstrates maximum

intensity in the ultraviolet region rather than Br and Cl based perovskites. The width of the absorption peak of $CsPbI_3$ is higher than that of $CsPbCl_3$ and $CsPbBr_3$ in the UV region. The first peak of α indicates the optical transition of electrons from Cl-3p of the valence band to Pb-6p of the conduction band at higher energy compared to that of the interband transitions of electrons in the case of $CsPbBr_3$ and $CsPbI_3$. The optical band gaps can be seen from the absorption peaks of the corresponding materials as E_g ($CsPbCl_3$) > E_g ($CsPbBr_3$) > E_g ($CsPbI_3$), which was consistent with the calculated values of E_g of $CsPbX_3$ perovskites (Table 4). The highest absorption peaks for all the materials occurred at the same energy of 14.6 eV (Fig. 8(a)).

Fig. 8(b) shows the pressure-dependent real part of the photoconductivity. From the figure, it was evident that when the absorption of photons was enhanced, the rate of photoconductivity tended to increase. Thereby, greater absorption and photoconductivity could be observed in the I-based perovskite compound relative to the Br- and Cl-based perovskite compounds with applied pressures. The photoconductivity comparison of these materials showed some peaks over a wide range of the energy spectrum. The conductivity initiatives and the first peaks could be ordered in terms of the energy as σ ($CsPbI_3$) > σ ($CsPbBr_3$) > σ ($CsPbCl_3$). The photoconductivity increased at the energy edges 4.2, 7.8, 11.3, and 14.1 eV for $CsPbCl_3$; 3.8, 7.3, 10.2, and 14.1 eV for $CsPbBr_3$; and 3.0, 6.4, 8.3, and 14.1 eV for $CsPbI_3$ as a result of the photonic energy absorption, which is shown in Fig. 8(b).

Reflectivity is an important optical property that determines the surface nature of materials for optoelectronic and solar cell applications.[92] Fig. 9(a) shows the pressure-dependent reflectivity spectra of the $CsPbX_3$ perovskites. From these graphs, it could be seen that at zero pressure the reflectivity was very low for all the studied cubic perovskite compounds. However, the reflectivity was the maximum for $CsPbI_3$ and the minimum for $CsPbCl_3$ perovskites, respectively. There were also some peaks that appeared in each spectrum that were the responses that still held true for the infra-red and visible regions. In the visible region, the first peaks were observed at 4.2, 3.8, and 3.3 eV for $CsPbCl_3$, $CsPbBr_3$, and $CsPbI_3$, respectively. Some other peaks appeared at 7.8, 11.5, 15.6, and 20.4 eV for $CsPbCl_3$; at 7.3, 10.9, 15.4, for $CsPbBr_3$; and at 6.3, 9.0, 11.3, 15.8 eV for $CsPbI_3$. From a comparison of the reflectivity, it could be clearly seen that $CsPbI_3$ showed the most homogeneous responses over a wide energy range in the ultraviolet region. When pressure was applied, the values of the reflectivity and loss function increased significantly with the increased applied pressure in the UV region.

4. Conclusions

Hydrostatic pressure's effects on the cubic perovskites $CsPbX_3$ were studied by DFT. All the direct band gap materials mentioned here showed a red-shifted nature of the electronic and optical band gap. The application of pressure resulted in strong attractive interaction between the valence band and the conduction band. The increment of pressure caused more overlapping of the CB and VB; whereby the semiconductor perovskites appeared as conductor after a certain amount pressure was applied. The electronic as well as optical responses were enhanced without any deformation of the crystal structure. Our investigation can expand the practical utilization of metal-halide perovskites in optoelectronics, photovoltaics, and quantum dot applications.

Author contributions

M. Aktary performed conceptualization, design the study, interpreted the data, and wrote the manuscript. M. Kamruzzaman helped to study, data analysis and wrote the manuscript. R. Afrose helped to understand software, DFT calculations, data curation, writing-review, write and editing the manuscript.

Conflicts of interest

The authors declare no competing financial interests.

Acknowledgements

The authors would like to thank Department of Physics, Begum Rokeya University, Rangpur, Bangladesh for supporting the computer facility. The research was funded by The Ministry of Science and Technology, Bangladesh. Authors are expressing gratitude to American Physical Society (APS) for appreciating this research. The author is dedicating this article to her beloved friends Popy, Pritha, and Dana.

References

1 A. Hagfeldt, G. Boschloo, L. Sun, L. Kloo and H. Pettersson, Dye-Sensitized Solar Cells, *Chem. Rev.*, 2010, **110**, 6595–6663.
2 J. H. Bang and P. V. Kamat, Quantum Dot Sensitized Solar Cells. A Tale of Two Semiconductor Nanocrystals: CdSe and CdTe, *ACS Nano*, 2009, **3**, 1467–1476.
3 T. R. Cook, *et al.*, Solar Energy Supply and Storage for the Legacy and Nonlegacy Worlds, *Chem. Rev.*, 2010, **110**, 6474–6502.
4 C.-H. Chiang, M. K. Nazeeruddin, M. Grätzel and C.-G. Wu, The synergistic effect of H $_2$ O and DMF towards stable and 20% efficiency inverted perovskite solar cells, *Energy Environ. Sci.*, 2017, **10**, 808–817.
5 M. M. Lee, J. Teuscher, T. Miyasaka, T. N. Murakami and H. J. Snaith, Efficient Hybrid Solar Cells Based on Meso-Superstructured Organometal Halide Perovskites, *Science*, 2012, **338**, 643–647.
6 N. J. Jeon, *et al.*, Compositional engineering of perovskite materials for high-performance solar cells, *Nature*, 2015, **517**, 476–480.
7 A. Yella, *et al.*, Porphyrin-Sensitized Solar Cells with Cobalt (II/III)–Based Redox Electrolyte Exceed 12 Percent Efficiency, *Science*, 2011, **334**, 629–634.

8 H.-J. Park, *et al.*, Inverted Organic Solar Cells with ZnO Thin Films Prepared by Sol–Gel Method, *J. Nanoelectron. Optoelectron.*, 2010, **5**, 135–138.
9 W. B. Xiao, M. M. Liu and C. Yan, Extracting and Studying Solar Cell Five Parameters Based on Lambert W Function, *J. Nanoelectron. Optoelectron.*, 2017, **12**, 189–195.
10 M. Liu, M. B. Johnston and H. J. Snaith, Efficient planar heterojunction perovskite solar cells by vapour deposition, *Nature*, 2013, **501**, 395–398.
11 J. Burschka, *et al.*, Sequential deposition as a route to high-performance perovskite-sensitized solar cells, *Nature*, 2013, **499**, 316–319.
12 M. Jørgensen, K. Norrman and F. C. Krebs, Stability/degradation of polymer solar cells, *Sol. Energy Mater. Sol. Cells*, 2008, **92**, 686–714.
13 Z. Pan, *et al.*, Near Infrared Absorption of $CdSe_x$ Te_{1-x} Alloyed Quantum Dot Sensitized Solar Cells with More than 6% Efficiency and High Stability, *ACS Nano*, 2013, **7**, 5215–5222.
14 M. D. Kelzenberg, *et al.*, Enhanced absorption and carrier collection in Si wire arrays for photovoltaic applications, *Nat. Mater.*, 2010, **9**, 239–244.
15 K. Yoshikawa, *et al.*, Silicon heterojunction solar cell with interdigitated back contacts for a photoconversion efficiency over 26%, *Nat. Energy*, 2017, **2**, 17032.
16 J. F. Geisz, *et al.*, Six-junction III–V solar cells with 47.1% conversion efficiency under 143 Suns concentration, *Nat. Energy*, 2020, **5**, 326–335.
17 A. M. M. Tanveer Karim, *et al.*, Structural, opto-electronic characteristics and second harmonic generation of solution processed CH3NH3PbI3-xClx thin film prepared by spray pyrolysis, *Mater. Sci. Eng., B*, 2020, **259**, 114599.
18 A. Kojima, K. Teshima, Y. Shirai and T. Miyasaka, Organometal Halide Perovskites as Visible-Light Sensitizers for Photovoltaic Cells, *J. Am. Chem. Soc.*, 2009, **131**, 6050–6051.
19 M. Jošt, *et al.*, Textured interfaces in monolithic perovskite/silicon tandem solar cells: advanced light management for improved efficiency and energy yield, *Energy Environ. Sci.*, 2018, **11**, 3511–3523.
20 P. Ramasamy, *et al.*, All-inorganic cesium lead halide perovskite nanocrystals for photodetector applications, *Chem. Commun.*, 2016, **52**, 2067–2070.
21 Q. A. Akkerman, *et al.*, Strongly emissive perovskite nanocrystal inks for high-voltage solar cells, *Nat. Energy*, 2016, **2**, 16194.
22 W.-J. Yin, T. Shi and Y. Yan, Unique Properties of Halide Perovskites as Possible Origins of the Superior Solar Cell Performance, *Adv. Mater.*, 2014, **26**, 4653–4658.
23 K. P. Marshall, M. Walker, R. I. Walton and R. A. Hatton, Enhanced stability and efficiency in hole-transport-layer-free CsSnI3 perovskite photovoltaics, *Nat. Energy*, 2016, **1**, 16178.
24 A. Swarnkar, *et al.*, Quantum dot–induced phase stabilization of α-$CsPbI_3$ perovskite for high-efficiency photovoltaics, *Science*, 2016, **354**, 92–95.
25 W. Zhang, G. E. Eperon and H. J. Snaith, Metal halide perovskites for energy applications, *Nat. Energy*, 2016, **1**, 16048.
26 Sandeep, *et al.*, Study of electronic and magnetic properties in 4 *f* electron based cubic $EuAlO_3$: a first-principles calculation, *Phys. Scr.*, 2015, **90**, 065803.
27 S. Chettri, *et al.*, GGA + U and mBJ + U study of the optoelectronic, magnetic and thermoelectric properties of the $SmAlO_3$ compound with spin–orbit coupling, *Int. J. Mod. Phys. B*, 2016, **30**, 1650078.
28 Sandeep, *et al.*, A first principles study of Nd doped cubic LaAlO3 perovskite: mBJ + U study, *J. Magn. Magn. Mater.*, 2016, **417**, 313–320.
29 D. P. Rai, *et al.*, Electronic and optical properties of cubic SrHfO3 at different pressures: A first principles study, *Mater. Chem. Phys.*, 2017, **186**, 620–626.
30 G. Murtaza and I. Ahmad, First principle study of the structural and optoelectronic properties of cubic perovskites CsPbM3 (M = Cl, Br, I), *Phys. B*, 2011, **406**, 3222–3229.
31 L. Lang, J.-H. Yang, H.-R. Liu, H. J. Xiang and X. G. Gong, First-principles study on the electronic and optical properties of cubic ABX3 halide perovskites, *Phys. Lett. A*, 2014, **378**, 290–293.
32 J. Qiu, *et al.*, All-solid-state hybrid solar cells based on a new organometal halide perovskite sensitizer and one-dimensional TiO2 nanowire arrays, *Nanoscale*, 2013, **5**, 3245.
33 H. J. Snaith, Perovskites: The Emergence of a New Era for Low-Cost, High-Efficiency Solar Cells, *J. Phys. Chem. Lett.*, 2013, **4**, 3623–3630.
34 H.-S. Kim, *et al.*, Lead Iodide Perovskite Sensitized All-Solid-State Submicron Thin Film Mesoscopic Solar Cell with Efficiency Exceeding 9%, *Sci. Rep.*, 2012, **2**, 591.
35 Z. Ku, Y. Rong, M. Xu, T. Liu and H. Han, Full Printable Processed Mesoscopic CH3NH3PbI3/TiO2 Heterojunction Solar Cells with Carbon Counter Electrode, *Sci. Rep.*, 2013, **3**, 3132.
36 C. Katan, N. Mercier and J. Even, Quantum and Dielectric Confinement Effects in Lower-Dimensional Hybrid Perovskite Semiconductors, *Chem. Rev.*, 2019, **119**, 3140–3192.
37 M. A. Fadla, B. Bentria, T. Dahame and A. Benghia, First-principles investigation on the stability and material properties of all-inorganic cesium lead iodide perovskites CsPbI3 polymorphs, *Phys. B*, 2020, **585**, 412118.
38 Z.-K. Tan, *et al.*, Bright light-emitting diodes based on organometal halide perovskite, *Nat. Nanotechnol.*, 2014, **9**, 687–692.
39 H. Zhu, *et al.*, Lead halide perovskite nanowire lasers with low lasing thresholds and high quality factors, *Nat. Mater.*, 2015, **14**, 636–642.
40 C. C. Stoumpos, *et al.*, Crystal Growth of the Perovskite Semiconductor $CsPbBr_3$: A New Material for High-Energy Radiation Detection, *Cryst. Growth Des.*, 2013, **13**, 2722–2727.
41 J. Deng, J. Li, Z. Yang and M. Wang, All-inorganic lead halide perovskites: a promising choice for photovoltaics and detectors, *J. Mater. Chem. C Mater.*, 2019, **7**, 12415–12440.
42 X. Li, *et al.*, All-Inorganic $CsPbBr_3$ Perovskite Solar Cells with 10.45% Efficiency by Evaporation-Assisted Deposition and Setting Intermediate Energy Levels, *ACS Appl. Mater. Interfaces*, 2019, **11**, 29746–29752.

43 H. Zhang, *et al.*, Centimeter-Sized Inorganic Lead Halide Perovskite $CsPbBr_3$ Crystals Grown by an Improved Solution Method, *Cryst. Growth Des.*, 2017, **17**, 6426–6431.
44 D. N. Dirin, I. Cherniukh, S. Yakunin, Y. Shynkarenko and M. V. Kovalenko, Solution-Grown $CsPbBr_3$ Perovskite Single Crystals for Photon Detection, *Chem. Mater.*, 2016, **28**, 8470–8474.
45 P. Ramasamy, *et al.*, All-inorganic cesium lead halide perovskite nanocrystals for photodetector applications, *Chem. Commun.*, 2016, **52**, 2067–2070.
46 Y. Lee, *et al.*, High-Performance Perovskite-Graphene Hybrid Photodetector, *Adv. Mater.*, 2015, **27**, 41–46.
47 Y. Wang, *et al.*, Hybrid Graphene-Perovskite Phototransistors with Ultrahigh Responsivity and Gain, *Adv. Opt. Mater.*, 2015, **3**, 1389–1396.
48 W. Nie, *et al.*, High-efficiency solution-processed perovskite solar cells with millimeter-scale grains, *Science*, 2015, **347**, 522–525.
49 M. A. Green, A. Ho-Baillie and H. J. Snaith, The emergence of perovskite solar cells, *Nat. Photonics*, 2014, **8**, 506–514.
50 G. Xing, *et al.*, Long-Range Balanced Electron- and Hole-Transport Lengths in Organic-Inorganic CH_3 NH_3 PbI_3, *Science*, 2013, **342**, 344–347.
51 X. Li, *et al.*, All Inorganic Halide Perovskites Nanosystem: Synthesis, Structural Features, Optical Properties and Optoelectronic Applications, *Small*, 2017, **13**, 1603996.
52 X. Li, *et al.*, Intercrossed Carbon Nanorings with Pure Surface States as Low-Cost and Environment-Friendly Phosphors for White-Light-Emitting Diodes, *Angew. Chem., Int. Ed.*, 2015, **54**, 1759–1764.
53 J. Song, *et al.*, Quantum Dot Light-Emitting Diodes Based on Inorganic Perovskite Cesium Lead Halides ($CsPbX_3$), *Adv. Mater.*, 2015, **27**, 7162–7167.
54 K. Lin, *et al.*, Perovskite light-emitting diodes with external quantum efficiency exceeding 20 per cent, *Nature*, 2018, **562**, 245–248.
55 Y. Wang, *et al.*, All-Inorganic Colloidal Perovskite Quantum Dots: A New Class of Lasing Materials with Favorable Characteristics, *Adv. Mater.*, 2015, **27**, 7101–7108.
56 Q. Zhang, *et al.*, Advances in Small Perovskite-Based Lasers, *Small Methods*, 2017, **1**, 1700163.
57 R. J. Sutton, *et al.*, Bandgap-Tunable Cesium Lead Halide Perovskites with High Thermal Stability for Efficient Solar Cells, *Adv. Energy Mater.*, 2016, **6**, 1502458.
58 E. M. Sanehira, *et al.*, Enhanced mobility $CsPbI_3$ quantum dot arrays for record-efficiency, high-voltage photovoltaic cells, *Sci. Adv.*, 2017, **3**, DOI: **10.1126/sciadv.aao4204**.
59 J. Li, *et al.*, 50-Fold EQE Improvement up to 6.27% of Solution-Processed All-Inorganic Perovskite $CsPbBr_3$ QLEDs via Surface Ligand Density Control, *Adv. Mater.*, 2017, **29**, 1603885.
60 N. Pandey, A. Kumar and S. Chakrabarti, Investigation of the structural, electronic, and optical properties of Mn-doped $CsPbCl_3$: theory and experiment, *RSC Adv.*, 2019, **9**, 29556–29565.
61 L. Protesescu, *et al.*, Nanocrystals of Cesium Lead Halide Perovskites ($CsPbX_3$, X = Cl, Br, and I): Novel Optoelectronic Materials Showing Bright Emission with Wide Color Gamut, *Nano Lett.*, 2015, **15**, 3692–3696.
62 O. Yu Posudievsky, *et al.*, Structural and Spectral Characteristics of Mechanochemically Prepared CsPbBr3, *Theor. Exp. Chem.*, 2017, **53**, 235–243.
63 M. Coduri, *et al.*, Origin of pressure-induced band gap tuning in tin halide perovskites, *Mater. Adv.*, 2020, **1**, 2840–2845.
64 M. I. Kholil and M. T. H. Bhuiyan, Effects of pressure on narrowing the band gap, visible light absorption, and semimetallic transition of lead-free perovskite CsSnBr3 for optoelectronic applications, *J. Phys. Chem. Solids*, 2021, **154**, 110083.
65 G. Liu, L. Kong, W. Yang and H. Mao, Pressure engineering of photovoltaic perovskites, *Mater. Today*, 2019, **27**, 91–106.
66 Y. Li, *et al.*, Electrical transport properties of Weyl semimetal WTe2 under high pressure, *J. Mater. Sci.*, 2020, **55**, 14873–14882.
67 J.-H. Lee, A. Jaffe, Y. Lin, H. I. Karunadasa and J. B. Neaton, Origins of the Pressure-Induced Phase Transition and Metallization in the Halide Perovskite $(CH_3NH_3)PbI_3$, *ACS Energy Lett.*, 2020, **5**, 2174–2181.
68 O. V. Oyelade, *et al.*, Pressure-Assisted Fabrication of Perovskite Solar Cells, *Sci. Rep.*, 2020, **10**, 7183.
69 S. Yalameha, P. Saeidi, Z. Nourbakhsh, A. Vaez and A. Ramazani, Insight into the topological phase and elastic properties of halide perovskites $CsSnX_3$ (X = l, Br, Cl) under hydrostatic pressures, *J. Appl. Phys.*, 2020, **127**, 085102.
70 R. Y. Alyoubi, B. M. Raffah, F. Hamioud and A. A. Mubarak, Effect of pressure on the mechanical, electronic and optical characters of $CsSnBr_3$ and $CsSnI_3$: *ab-initio* study, *Mod. Phys. Lett. B*, 2021, **35**, 2150056.
71 G. Xiao, *et al.*, Pressure Effects on Structure and Optical Properties in Cesium Lead Bromide Perovskite Nanocrystals, *J. Am. Chem. Soc.*, 2017, **139**, 10087–10094.
72 S. J. Clark, *et al.*, First principles methods using CASTEP, *Z Kristallogr Cryst. Mater.*, 2005, **220**, 567–570.
73 W. Kohn and L. J. Sham, Self-Consistent Equations Including Exchange and Correlation Effects, *Phys. Rev.*, 1965, **140**, A1133–A1138.
74 P. Hohenberg and W. Kohn, Inhomogeneous Electron Gas, *Phys. Rev.*, 1964, **136**, B864–B871.
75 S. Idrissi, H. Labrim, S. Ziti and L. Bahmad, Investigation of the physical properties of the equiatomic quaternary Heusler alloy CoYCrZ (Z = Si and Ge): a DFT study, *Appl. Phys. A*, 2020, **126**, 190.
76 S. Idrissi, H. Labrim, S. Ziti and L. Bahmad, Structural, electronic, magnetic properties and critical behavior of the equiatomic quaternary Heusler alloy CoFeTiSn, *Phys. Lett. A*, 2020, **384**, 126453.
77 S. Idrissi, H. Labrim, S. Ziti and L. Bahmad, Characterization of the Equiatomic Quaternary Heusler Alloy ZnCdRhMn: Structural, Electronic, and Magnetic Properties, *J Supercond Nov Magn*, 2020, **33**, 3087–3095.
78 J. Hutton, R. J. Nelmes, G. M. Meyer and V. R. Eiriksson, High-resolution studies of cubic perovskites by elastic

neutron diffraction: $CsPbCl_3$, *J. Phys. C-Solid State Phys.*, 1979, **12**, 5393–5410.

79 M. Aktary, M. Kamruzzaman and R. Afrose, A comparative study of the mechanical stability, electronic, optical and photocatalytic properties of $CsPbX_3$ (X = Cl, Br, I) by DFT calculations for optoelectronic applications, *RSC Adv.*, 2022, **12**, 23704–23717.

80 M. M. Lee, J. Teuscher, T. Miyasaka, T. N. Murakami and H. J. Snaith, Efficient Hybrid Solar Cells Based on Meso-Superstructured Organometal Halide Perovskites, *Science*, 2012, **338**, 643–647.

81 M. Jørgensen, K. Norrman and F. C. Krebs, Stability/degradation of polymer solar cells, *Sol. Energy Mater. Sol. Cells*, 2008, **92**, 686–714.

82 K. Yoshikawa, *et al.*, Silicon heterojunction solar cell with interdigitated back contacts for a photoconversion efficiency over 26%, *Nat. Energy*, 2017, **2**, 17032.

83 M. D. Kelzenberg, *et al.*, Enhanced absorption and carrier collection in Si wire arrays for photovoltaic applications, *Nat. Mater.*, 2010, **9**, 239–244.

84 T. Paul, *et al.*, Tunable cathodoluminescence over the entire visible window from all-inorganic perovskite $CsPbX_3$ 1D architecture, *J. Mater. Chem. C Mater.*, 2018, **6**, 3322–3333.

85 M. Aktary, *et al.*, Mechanical and optoelectronic properties of ternary telluride NbFeTe2: A DFT approach, *Comput. Condensed Matter.*, 2023, **34**, e00788.

86 G. E. Eperon, *et al.*, Formamidinium lead trihalide: a broadly tunable perovskite for efficient planar heterojunction solar cells, *Energy Environ. Sci.*, 2014, **7**, 982.

87 L. Lang, *et al.*, Three-step approach for computing band offsets and its application to inorganicABX_3 halide perovskites, *Phys. Rev. B: Condens. Matter Mater. Phys.*, 2015, **92**, 075102.

88 K. Heidrich, *et al.*, Electronic structure, photoemission spectra, and vacuum-ultraviolet optical spectra of $CsPbCl_3$ and CsPbBr3, *Phys. Rev. B: Condens. Matter Mater. Phys.*, 1981, **24**, 5642–5649.

89 R. J. Sutton, *et al.*, Bandgap-Tunable Cesium Lead Halide Perovskites with High Thermal Stability for Efficient Solar Cells, *Adv. Energy Mater.*, 2016, **6**, 1502458.

90 J. B. Hoffman, A. L. Schleper and P. V. Kamat, Transformation of Sintered $CsPbBr_3$ Nanocrystals to Cubic $CsPbI_3$ and Gradient $CsPbBr_x I_{3-x}$ through Halide Exchange, *J. Am. Chem. Soc.*, 2016, **138**, 8603–8611.

91 L. Lang, *et al.*, Three-step approach for computing band offsets and its application to inorganic ABX_3 halide perovskites, *Phys. Rev. B: Condens. Matter Mater. Phys.*, 2015, **92**, 075102.

92 Md. S. Hossain, A. S. Roy and Md. S. Islam, In silico analysis predicting effects of deleterious SNPs of human RASSF5 gene on its structure and functions, *Sci. Rep.*, 2020, **10**, 14542.